

# Quantum magnetism of ultracold fermions in an optical lattice

Daniel Greif,<sup>1</sup> Thomas Uehlinger,<sup>1</sup> Gregor Jotzu,<sup>1</sup> Leticia Tarruell,<sup>1,2</sup> and Tilman Esslinger<sup>1</sup>

<sup>1</sup>*Institute for Quantum Electronics, ETH Zurich, 8093 Zurich, Switzerland*

<sup>2</sup>*LP2N UMR 5298, Univ. Bordeaux 1, Institut d'Optique and CNRS, 351 cours de la Libération, 33405 Talence, France*

Quantum magnetism lies at the heart of many intriguing phenomena in condensed matter physics. Its manifestations range from antiferromagnets to spin-liquids, and it is believed to play a central role in high-temperature superconductivity<sup>1–3</sup>. Remarkably, even simple models of the underlying many-body physics are often intractable with current theoretical and computational methods. The controlled setting of ultracold fermionic atoms in optical lattices is therefore regarded as a promising route to provide new insights<sup>4–6</sup>. Yet, the low temperature scale required for entering the regime of quantum magnetism has hindered progress for optical lattice based systems. So far, superexchange oscillations on isolated double wells, one-dimensional decoupled Ising spin chains and classical magnetism on a triangular lattice were studied with bosonic quantum gases<sup>7–9</sup>. Here we report on the observation of quantum magnetism of a Fermi gas in an optical lattice. The key to obtaining and detecting the short-range magnetic order is a tunable geometry optical lattice. When loading a low-temperature two-component gas with repulsive interactions into either a dimerized or anisotropic simple cubic lattice, we find magnetic correlations on neighbouring sites. The correlations manifest as an excess number of singlets as compared to triplets consisting of two atoms with opposite spins. For the anisotropic lattice, we determine the transverse spin correlator from the singlet-triplet imbalance and observe antiferromagnetic correlations along one spatial axis.

Ultracold Fermi gases with repulsive interactions in optical lattices are an almost ideal realization of the Fermi-Hubbard model<sup>10</sup>, having the potential to emulate its elusive low-temperature phase diagram. While density ordering has been explored experimentally in the metal-Mott insulator transition<sup>11,12</sup>, spin ordering has so far not been observed owing to the low temperatures required. The physics of the low-energy Hubbard sector is determined by the interplay of kinetic energy, inter-particle interactions and spin ordering, which is essential to antiferromagnetic order, resonating valence-bond states, pseudo-gap physics and spin liquids<sup>1–3,13</sup>.

In this work, we use a tunable geometry optical lattice<sup>14,15</sup> to both access the low energy sector of the Hubbard model and probe magnetic correlations. A central requirement for quantum magnetism are temperatures below the exchange energy associated with spin or-

dering. The atoms are either prepared in a dimerized or an anisotropic simple cubic lattice, as shown in Fig. 1. In both geometries, a subset of links of the underlying simple cubic lattice is set to a larger exchange energy as compared to the other links. This determines the character of magnetic order<sup>13</sup> and, given a fixed total entropy, allows for temperatures between the two exchange energy scales. In the dimerized lattice the resulting correlations on the strong links correspond to an excess population of the low energy singlet as compared to the triplet state. In the anisotropic lattice the low temperatures lead to antiferromagnetic spin correlations, the transverse component of which is also detected via a singlet-triplet imbalance.

The experiment is performed with a harmonically confined, balanced two-component mixture of a quantum degenerate Fermi gas of <sup>40</sup>K. The atoms are prepared in two magnetic sublevels  $m_F = -9/2, -7/2$  of the  $F = 9/2$  hyperfine manifold, denoted by  $\uparrow$  and  $\downarrow$ , at temperatures below 10% of the Fermi temperature. We load 50,000 – 100,000 repulsively interacting atoms at an  $s$ -wave scattering length of 106(1)  $a_0$  into the three-dimensional optical lattice, where  $a_0$  denotes the Bohr radius. The lattice is created by a combination of interfering laser beams operating at 1064 nm with lattice depths

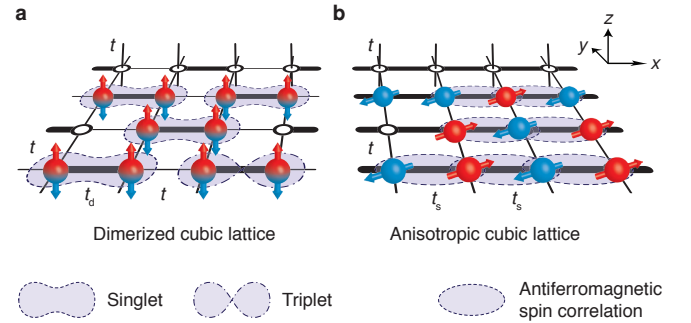


**FIG. 1. Magnetic spin correlations.** Schematic view of the nearest-neighbour spin correlations observed in the experiment. A two-component mixture of fermionic atoms (red and blue) is prepared close to half-filling in a cubic lattice with two different tunnel coupling configurations. **a**, Dimerized lattice with the strong dimer links  $t_d$  and weaker links  $t$ . Low temperatures lead to an excess number of singlets over triplets. **b**, Anisotropic lattice with strong and weak tunnelling  $t_s$  and  $t$  along different spatial axes. Antiferromagnetic spin correlations in the transverse direction are formed along the strong link direction. In both figures exemplary thermal excitations in the form of spin excitations or holes are shown.

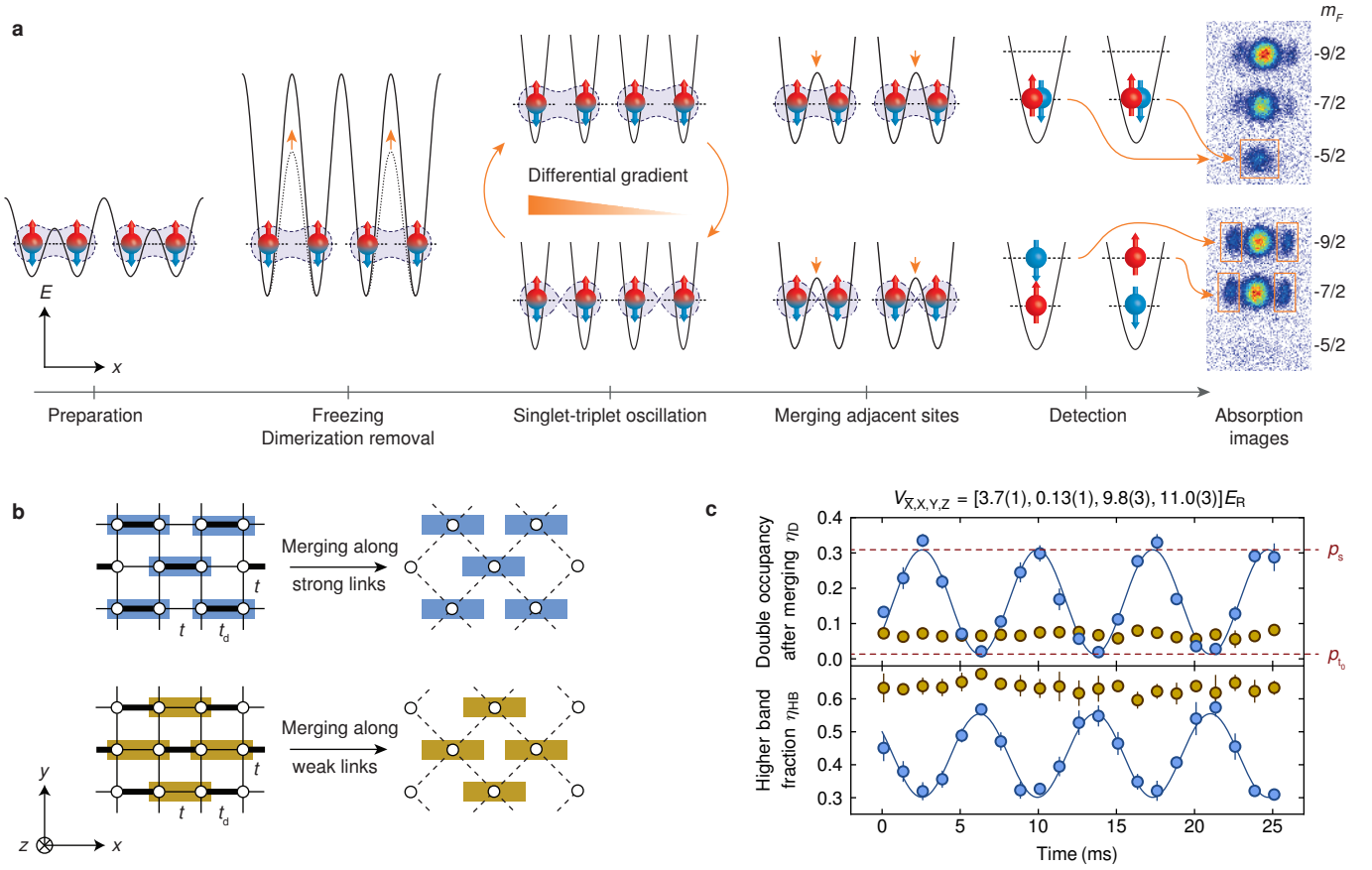


**FIG. 2. Detection scheme.** Summary of the technique used for measuring the atomic singlet and triplet fractions  $p_s$  and  $p_{t_0}$ . **a**, Schematic view of the different detection steps for the exemplary case of two singlet states in a dimerized lattice. Depending on the oscillation time, the absorption images on the right show either a large double occupancy corresponding to singlets (top row), or an increased higher band fraction indicating triplet states (bottom row). **b**, The two possible merging configurations in a dimerized lattice. Singlets and triplets are detected on a set of adjacent sites arranged on a chequerboard pattern in the plane. **c**, Exemplary singlet-triplet oscillation in a strongly dimerized lattice with  $U/t = 11.0(8)$  and  $t_d/t = 22(2)$ . We observe an oscillation in the double occupancy after merging,  $\eta_D$ , and in the higher band fraction,  $\eta_{HB}$ , when merging along the strong links (blue data), whereas no oscillations are visible for the weak links (ochre data). The phase of the oscillation is shifted owing to the double occupancy removal procedure (Methods). The red dashed lines denote the extracted singlet and triplet fraction  $p_s$  and  $p_{t_0}$ . Error bars show the standard deviation of at least five measurements.

$V_{\bar{X}}$ ,  $V_X$ ,  $V_Y$  and  $V_Z$  (Methods). We independently control the tunnelling strengths along all three spatial axes. In addition we can introduce a chequerboard dimerization in the  $xy$  plane by strengthening every second tunnelling link along the  $x$  axis, see Fig. 1a. The chequerboard pattern replicates along the  $z$  axis. Our system is well described by a three-dimensional single-band Hubbard model with repulsive on-site interaction energy  $U$ , unless explicitly stated. The tunnelling along the weak links in both lattice geometries is set to  $t/h = 67(3)$  Hz for all measurements, where  $h$  denotes Planck's constant.

As shown in Fig. 2a and b, the fraction of atoms forming singlets and triplets on neighbouring lattice sites ( $p_s$  and  $p_{t_0}$ ) is detected by transforming the lattice to a chequerboard geometry, similar to a previously developed technique<sup>16</sup>. In the dimerized lattice our detection scheme locally projects onto the two-site eigenstates of isolated dimers, whereas for the anisotropic lattice the

singlet state is directly projected onto  $(|\uparrow, \downarrow\rangle - |\downarrow, \uparrow\rangle)/\sqrt{2}$  (Methods). In the first detection step, the atomic motion in the initial lattice is frozen by rapid conversion to a simple cubic structure with negligible tunnelling. Next, all atoms on doubly occupied sites are removed. We then apply a magnetic field gradient, which creates a differential bias energy  $\Delta$  for atoms of opposite spins on adjacent sites and causes coherent oscillations between the singlet  $|s\rangle = (|\uparrow, \downarrow\rangle - |\downarrow, \uparrow\rangle)/\sqrt{2}$  and the triplet  $|t_0\rangle = (|\uparrow, \downarrow\rangle + |\downarrow, \uparrow\rangle)/\sqrt{2}$  state at a frequency  $\nu = \Delta/h$ . If the initial amount of singlets and triplets is equal, no overall oscillation will be visible, as  $|s\rangle$  and  $|t_0\rangle$  oscillate in antiphase.

After a certain oscillation time, we remove the gradient and merge two adjacent sites. Owing to the symmetry of the two-particle wavefunction, the singlet state on neighbouring sites evolves to a doubly occupied site with both

atoms in the lowest band, while the triplet state transforms into a state with one atom in the lowest and one atom in the first excited band. The fraction of atoms on doubly occupied sites  $\eta_D$  in the merged lattice is detected by a radiofrequency transfer to the previously unpopulated  $m_F = -5/2$  spin state<sup>11</sup>. The fraction of atoms in the higher band  $\eta_{HB}$  is obtained from a band mapping technique<sup>6</sup>. For the final readout we take absorption images after Stern-Gerlach separation of the spin states during ballistic expansion. For an imbalance between the initial singlet and triplet populations,  $\eta_D$  and  $\eta_{HB}$  will show oscillations with opposite amplitudes. As the double occupancy contains only contributions from two particles with opposite spins, we can infer the fraction of atoms forming singlets and triplets from the maxima and minima of a sinusoidal fit to  $\eta_D$ . The higher band fraction has an additional offset caused by dimers containing two atoms with the same spin or one atom with an antisymmetric spatial wavefunction.

When loading atoms into a strongly dimerized lattice and merging along the strong links, we observe oscillations in  $\eta_D$  and  $\eta_{HB}$ , see Fig. 2c. This reveals an excess number of singlets, corresponding to magnetic order on neighbouring sites. We quantify this order by the normalized imbalance

$$\mathcal{I} = \frac{p_s - p_{t_0}}{p_s + p_{t_0}}. \quad (1)$$

The order in the strongly dimerized lattice originates from temperatures below the intra-dimer exchange energy  $J_d = -U/2 + \sqrt{16t_d^2 + U^2}/2$ , which denotes the singlet-triplet splitting on a single dimer. While such temperatures require very low entropies for isotropic lattices<sup>17</sup>, in our system the access to the regime of magnetic ordering is facilitated by the presence of the weaker inter-dimer exchange energy  $J \ll J_d$ . This leads to an entropy redistribution from states on the strong to the weak links and gives access to the temperature regime  $J < k_B T < J_d$  for experimentally attainable entropies (here  $k_B$  denotes the Boltzmann constant). As expected for strong dimerization, we find no visible oscillations when merging along the weak links, which indicates the absence of magnetic correlations on these links, see Fig. 2c. The observed constant values of  $\eta_D = 0.07(1)$  and  $\eta_{HB} = 0.63(3)$  are consistent with a state where nearly all singlets are located on neighbouring dimer links, with vanishing correlations between them.

To analyse the effect of temperature on the magnetic correlations, we measure the dependence of the singlet-triplet imbalance on entropy, see Fig. 3a. The imbalance  $\mathcal{I}$  and the absolute singlet fraction  $p_s$  reduce for larger entropies, as triplet states become thermally populated. The singlet fraction is additionally diminished by a shrinking half-filled region in the trapped system<sup>18</sup>. We find good agreement with a second order high-temperature series expansion of coupled dimers when including an entropy increase of  $\Delta s = 0.4 k_B$  with respect to the initial entropy in the harmonic trap,  $s_{in}$ .

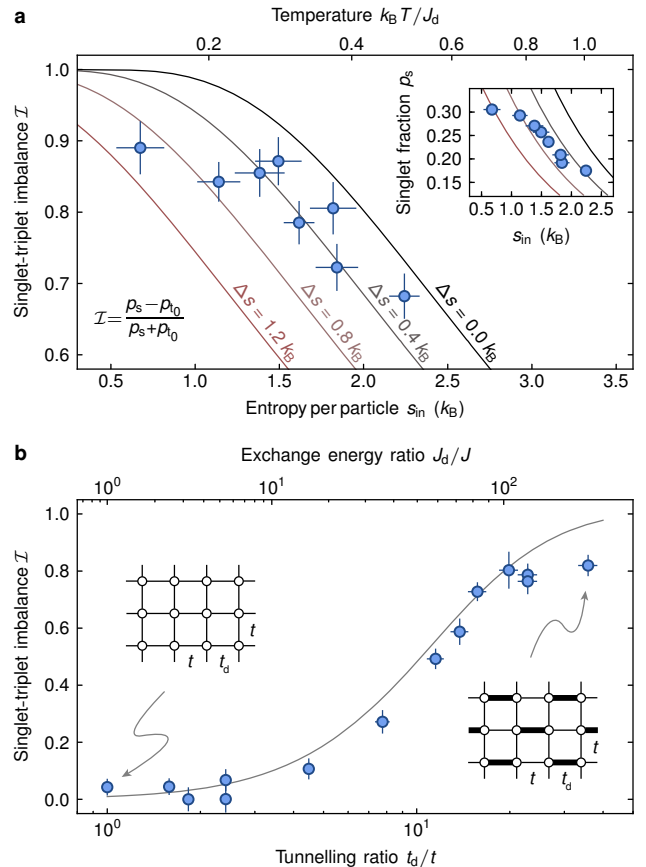


**FIG. 3. Dimerized simple cubic lattice.** **a**, Singlet-triplet imbalance on the strong dimer links vs. initial entropy before loading into the lattice  $s_{in}$  and temperature  $k_B T / J_d$  in a dimerized lattice with  $U/t = 11.0(8)$  and  $t_d/t = 22(2)$ . The imbalance and the absolute singlet fraction (inset) decrease with increasing entropy. Solid lines are the prediction of a high-temperature series expansion taking into account different amounts of added entropy  $\Delta s$  during the lattice loading. **b**, Imbalance versus dimerization  $t_d/t$  and  $J_d/J$ , showing an increase for strongly dimerized simple cubic lattices. The solid line is the theory prediction for an entropy per particle of  $1.8 k_B$  in the lattice, which includes the heating during loading. Vertical error bars denote the fit error from singlet-triplet oscillations consisting of 63 measurements, the errors in  $t_d/t$  stem from lattice calibration uncertainties and the errors in  $s_{in}$  are the standard deviation of five measurements. Individual curves of  $p_s$  and  $p_{t_0}$  for all measurements can be found in the Supplementary Information.

This heating is associated to the lattice loading<sup>19</sup> and is larger for the lowest entropies, consistent with previous results<sup>18</sup>. From the measured imbalances we infer temperatures below  $0.4 J_d$ .

For reduced dimerizations the coupling between dimers leads to increased inter-dimer correlations. The excitation energy of triplets is then lowered as they delocalize over the lattice, thus changing the nature of magnetic ordering. In Fig. 3b we use the tunable lattice to investigate the dependence of the imbalance  $\mathcal{I}$  on the tun-

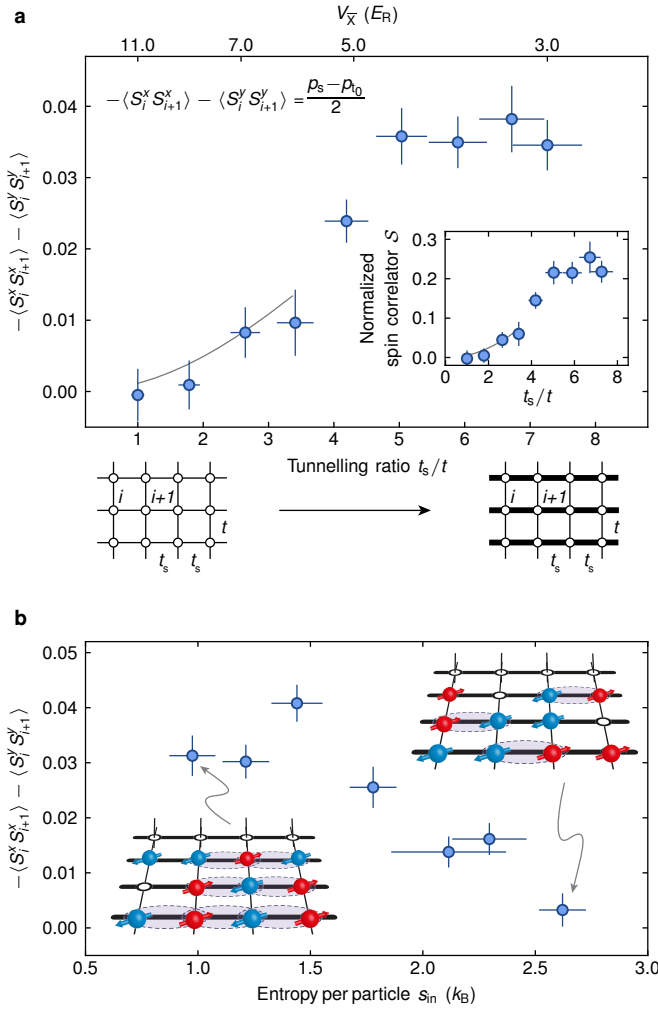


FIG. 4. **Nearest-neighbour antiferromagnetic order.** **a**, Transverse spin correlator versus tunnelling ratio  $t_s/t$  and lattice depth  $V_X$  in a three-dimensional anisotropic simple cubic lattice with  $V_{Y,Z} = 11.0(3) E_R$ . Positive values correspond to antiferromagnetic ordering. The inset shows the normalized spin correlator  $\mathcal{S}$ , denoting the fraction of antiferromagnetic ordering at the relevant density. Here  $U/t$  decreases from 16(1) to 10.5(8). Solid lines are the prediction of a high-temperature series expansion for an entropy per particle of  $1.8 k_B$ , as used in Fig. 3b, and are shown up to  $t_s/k_B T = 1/2$ . **b**, Transverse spin correlator versus entropy before loading into the lattice at  $U/t = 10.5(8)$  and  $t_s/t = 7.3(6)$ , together with a schematic view of the spin ordering. Error bars as in Fig. 3.

nelling ratio  $t_d/t$ . As the dimerization is progressively removed the imbalance decreases in good agreement with theory and eventually falls below our experimental resolution. This decrease can be attributed to the inter-dimer exchange energy  $J_d$  becoming smaller than the temperature  $T$ . For vanishing temperatures the system is expected to undergo a quantum phase transition from a spin-liquid state to a long-range ordered antiferromagnet as  $t_d/t$  is reduced below a critical value, where the spin gap becomes zero<sup>13,20</sup>.

The key to the observation of quantum magnetism in our system is the presence of two different exchange energy scales. Without dimerization, this situation also occurs for anisotropic simple cubic lattices with tunnelling  $t$  along two axes and a stronger tunnelling  $t_s$  along the third direction. In this case the symmetry between neighbouring links is restored and the detected singlet and triplet fractions are the same for both merging configurations. We observe a clear population difference  $(p_s - p_{t_0})/2$  after loading a gas with entropies  $s_{in}$  below  $1.0 k_B$  into an anisotropic lattice, which increases to 4% for larger tunnelling ratios  $t_s/t$ , see Fig. 4a. The population difference is equal to the transverse spin correlator between neighbouring sites  $i$  and  $i + 1$  along the strong tunnelling direction

$$-\langle S_i^x S_{i+1}^x \rangle - \langle S_i^y S_{i+1}^y \rangle = (p_s - p_{t_0})/2. \quad (2)$$

This quantity hence directly characterizes the fraction of atoms with antiferromagnetic ordering on neighbouring sites in the entire atomic cloud. Our observations also extend to weak lattices, where correction terms to the single-band Hubbard model become relevant<sup>21</sup>. In this regime a variety of magnetic phases have been predicted<sup>22,23</sup>.

The results can be compared to a second order high-temperature series expansion (Methods). We find good agreement in the regime of small anisotropies. For larger anisotropies the expansion breaks down, as the strong tunnelling and the temperature become comparable. In this regime we expect the temperature to lie between the large and small exchange scales  $J < k_B T < J_s$ . The system then behaves as an array of one-dimensional spin-ordered chains, without correlations between them<sup>24</sup>. Low-dimensional systems have been predicted to show enhanced nearest-neighbour correlations<sup>25</sup>.

For temperatures much larger than the strong exchange energy the magnetic correlations should disappear. In Fig. 4b we study the dependence on the initial entropy  $s_{in}$  and find the correlations to vanish above  $2.5 k_B$ , where  $k_B T \gg J_s$  is expected.

Owing to the presence of the harmonic trap, most spin correlated atoms are located in the centre, where the filling is close to one particle per site. The density-normalized fraction of antiferromagnetic ordering is obtained when dividing by the fraction of atoms with two particles of arbitrary spin on adjacent sites. Under the assumption that all spin correlators  $\langle S_i^{x,y,z} S_{i+1}^{x,y,z} \rangle$  are equal – which applies if all symmetry breaking fields are much smaller than all other energy scales – the normalized spin correlator  $\mathcal{S}$  can be directly obtained from the measurement of singlets and triplets (here  $n_i^s$  is one for a single particle of any spin on site  $i$  and zero otherwise)

$$\mathcal{S} = \frac{-4\langle S_i^z S_{i+1}^z \rangle}{\langle n_i^s n_{i+1}^s \rangle} = \frac{p_s - p_{t_0}}{p_s + 3p_{t_0}}. \quad (3)$$

The normalized antiferromagnetic correlations along the strong tunnelling direction reach 25%, see inset Fig. 4a. This corresponds to approximately 5,000 ordered atoms.

In this work, we have demonstrated the observation of quantum magnetism of repulsively interacting ultracold fermions in cubic lattices and investigated the dependence on temperature, lattice dimerization and anisotropy. The presented approach should also facilitate the access to low temperature regimes for two-dimensional geometries. Furthermore, the tunable geometry optical lattice allows the extension of our studies to spin-ladder systems, dimerized one-dimensional chains and zig-zag chains, where the interplay between quantum fluctuations and magnetic ordering plays a particularly important role<sup>24,26</sup>. At even lower temperatures, the existence of spin-liquids in honeycomb or triangular lattices could be investigated<sup>27</sup>.

## METHODS

### A. Preparation.

After sympathetic cooling with  $^{87}\text{Rb}$ ,  $2 \times 10^6$  fermionic  $^{40}\text{K}$  atoms are transferred into an optical dipole trap operating at a wavelength of 826 nm. A balanced incoherent spin mixture of atoms in the Zeeman levels  $m_F = -9/2$  and  $-7/2$  of the  $F = 9/2$  hyperfine manifold is then prepared and evaporatively cooled<sup>11</sup>. When taking data as a function of entropy, the gas is heated through inelastic losses by setting the magnetic bias field to a value close to the Feshbach resonance at 202.1 G. We measure the entropy per particle in the dipole trap  $s_{\text{in}}$  using Fermi fits to the momentum distribution of the cloud after expansion. The field is finally increased to 221.4 G resulting in a scattering length of 106(1)  $a_0$ . The optical lattice is subsequently turned on in 200 ms using a spline shaped laser-intensity ramp.

### B. Trapping potential.

The red-detuned optical lattice is created by four retro-reflected laser beams at  $\lambda = 1064\text{ nm}$  (refs 14 and 15). This gives rise to a potential of the form

$$\begin{aligned} V(x, y, z) = & -V_{\bar{X}} \cos^2(kx + \theta/2) - V_X \cos^2(kx) \\ & -V_Y \cos^2(ky) \\ & -2\alpha \sqrt{V_X V_Y} \cos(kx) \cos(ky) \cos \varphi \\ & -V_Z \cos^2(kz), \end{aligned} \quad (4)$$

where  $V_{\bar{X}}$ ,  $V_X$ ,  $V_Y$  and  $V_Z$  denote single-beam lattice depths (as calibrated using Raman-Nath diffraction on a  $^{87}\text{Rb}$  Bose-Einstein condensate),  $k = 2\pi/\lambda$  and the measured visibility of the interference pattern  $\alpha$  is 0.90(5). The phase  $\varphi$  is stabilized to 0.00(3) $\pi$ , whilst  $\theta$  is set to 1.000(1) $\pi$ . Gravitation points along the  $y$  direction.

The laser beams create an overall harmonic trapping potential which scales with the lattice depths according

to the approximate expressions

$$\begin{aligned} \omega_x & \propto \sqrt{V_Y + 1.11V_Z} \\ \omega_y & \propto \sqrt{V_{\bar{X}} + 0.81(V_X V_Y / V_{\bar{X}}) + 0.78V_Z} \\ \omega_z & \propto \sqrt{V_{\bar{X}} + 0.81(V_X V_Y / V_{\bar{X}}) + 1.24V_Y}. \end{aligned}$$

For  $V_{\bar{X},X,Y,Z} = [3.7(1), 0.13(1), 9.8(3), 11.0(3)] E_R$ , as in Fig. 3a, the lattice contributes trapping frequencies of  $\omega_{x,y,z}^{\text{Lattice}}/2\pi = [62.7(9), 57(1), 54.3(3)]$  Hz. Additionally, the optical dipole trap creates a trapping of  $\omega_{x,y,z}^{\text{Dipole}}/2\pi = [30.7(2), 105.9(3), 34.6(2)]$  Hz, in all data sets shown, except for Fig. 2c and 4a, where  $\omega_{x,y,z}^{\text{Dipole}}/2\pi = [28.1(2), 90.1(3), 31.6(2)]$  Hz.

### C. Detection lattice ramp.

For measurements in the dimerized lattice, the lattice is ramped up in two steps. All beam intensities are linearly increased over the course of 0.5 ms up to the point where  $V_Y = 30(1) E_R$ ,  $V_Z = 40(1) E_R$  and all other intensities in the  $xy$  plane are ramped such that the potential is not deformed. In a second linear ramp lasting 10 ms, the lattice is changed to a simple cubic geometry where  $V_{\bar{X},X,Y,Z} = [25(1), 0, 30(1), 40(1)] E_R$ .

Our observable locally projects onto the two-site eigenstates of individual dimers, which includes an admixture of double occupancies. We use an exact calculation of a two-site Hubbard model to estimate the adiabaticity of this ramp. The unnormalized singlet ground state of this system is given by

$$\frac{4t_d}{-U + \sqrt{16t_d^2 + U^2}} (|\uparrow, \downarrow\rangle - |\downarrow, \uparrow\rangle) + (|\uparrow\downarrow, 0\rangle + |0, \uparrow\downarrow\rangle).$$

There is hence a significant contribution of double occupancy in the regime where  $U \sim t_d$ , as applies for the most strongly dimerized lattices investigated in this paper, whilst the contribution vanishes for the deep simple cubic lattice used for detection where  $U/t \approx 600$ . For the given ramp-times and including site-offsets due to the harmonic trapping potential, the probability of populating excited states during such a ramp remains below 0.1% for all values of  $U$  and  $t_d$  explored in the dimerized systems.

In the anisotropic lattice, we directly ramp to  $V_{\bar{X},Y,Z} = [25(1), 30(1), 40(1)] E_R$  in 0.5 ms ( $V_X = 0 E_R$  throughout). Our detection method then corresponds to locally projecting the wavefunction of the system onto  $(|\uparrow, \downarrow\rangle - |\downarrow, \uparrow\rangle)/\sqrt{2}$  on pairs of sites when measuring  $p_s$ , hence excluding any contributions from double occupancies. The probability of this projection is above 80% for all shown data and is higher for deeper lattices. For both lattice geometries, the triplet state stays unaffected by changes in  $U$  and  $t$ .



### D. Singlet-triplet oscillations.

For both systems, once the ramp to the deep simple cubic lattice has been completed, double occupancies are removed via spin-changing collisions, which occur after transferring atoms from the  $m_F = -7/2$  to the  $m_F = -3/2$  state<sup>28</sup>. We verify that this procedure removes all double occupancies but leaves singly occupied sites unaffected by measuring the number of double occupancies and the total number of atoms before and after applying the removal sequence. A magnetic field gradient causing spin-dependent energy offsets of  $\Delta_{-9/2, -7/2}/h = [1291(1), 1156(1)]$  Hz between neighbouring sites is then applied, giving rise to coherent oscillations between singlets and triplets<sup>16</sup>. Subsequently, pairs of adjacent lattice sites are adiabatically merged into one by linearly reducing  $V_X$  to zero whilst increasing  $V_X$  to  $25(1) E_R$ . The double occupancy in the merged lattice is then measured as in ref. 11, but taking into account an independently calibrated detection efficiency of 89(2)%. We verify that merged sites containing two atoms of opposite spin but in different bands are not detected as double occupancies by artificially creating a state containing large amounts of triplets but no singlets and measuring  $\eta_D$ .

We apply a sinusoidal fit to the double occupancy where the frequency and phase are fixed and take into account the damping of the oscillations, which was calibrated independently and is included by multiplying the amplitude by 1.16. A phase shift arises owing to a weak residual magnetic field gradient present during the double occupancy removal procedure, whereas the contribution from switching the singlet-triplet oscillation gradient on and off is negligible. We confirm that the maximum of the oscillation corresponds to its starting point (and hence to the number of singlets) by merging the lattice immediately after it has been ramped to a deep simple cubic structure.

### E. Theoretical model

For sufficiently deep lattices the system is well described by a single band Fermi-Hubbard model, which is given by

$$\hat{H} = -t_{i,j} \sum_{\langle ij \rangle, \sigma} (\hat{c}_{i\sigma}^\dagger \hat{c}_{j\sigma} + \text{h.c.}) + U \sum_i \hat{n}_{i\uparrow} \hat{n}_{i\downarrow} \quad (5)$$

for a homogeneous system, using standard notation. The interaction energy  $U$  and nearest-neighbour tunnelling  $t_{i,j}$  are evaluated from Wannier function integrals<sup>4</sup>. The dimerized lattice theory curves are calculated from a perturbative coupling of isolated dimer links with tunnelling  $t$ . The resulting partition function expansion is then calculated up to second order in  $t/k_B T$ . While the dimer link contains 16 states in total and the tunnelling operator is non-diagonal between neighbouring dimers, the evaluation of the relevant matrix elements is directly analogous to the case of single sites<sup>29</sup>. The harmonic trap is included in a local density approximation, which leads to a quadratically varying chemical potential. All thermodynamic quantities are obtained after integration over the entire trap using independent calibrations of the atom number, trap frequencies and lattice depths<sup>19</sup>. In the limit of very strong dimerization, theory predicts  $p_{t_0}/p_s \propto \exp(-J_d/k_B T)$ , which can be used for lattice thermometry.

For the anisotropic lattice we evaluate the correlators  $\langle S_i^z S_{i+1}^z \rangle$  and  $\mathcal{S}$  in a second order series expansion of coupled single sites<sup>30</sup>. The thermodynamic observables are obtained in a similar way as previously described<sup>19</sup>, using the average tunnelling  $\sqrt{(t_s^2 + 2t^2)}/3$ . Equation 2 is computed by evaluating the matrix elements of the spin operators.

- 
- <sup>1</sup> Anderson, P. W. *et al.* The physics behind high-temperature superconducting cuprates: the ‘plain vanilla’ version of RVB. *J. Phys. Condens. Matter* **16**, R755–R769 (2004).
  - <sup>2</sup> Balents, L. Spin liquids in frustrated magnets. *Nature* **464**, 199–208 (2010).
  - <sup>3</sup> Auerbach, A. *Interacting Electrons and Quantum Magnetism*. Springer, New York (1998).
  - <sup>4</sup> Lewenstein, M. *et al.* Ultracold atomic gases in optical lattices: mimicking condensed matter physics and beyond. *Adv. Phys.* **56**, 243–379 (2007).
  - <sup>5</sup> Bloch, I., Dalibard, J. & Zwerger, W. Many-body physics with ultracold gases. *Rev. Mod. Phys.* **80**, 885–964 (2008).
  - <sup>6</sup> Esslinger, T. Fermi-Hubbard physics with atoms in an optical lattice. *Annu. Rev. Condens. Matter Phys.* **1**, 129–152 (2010).
  - <sup>7</sup> Trotzky, S. *et al.* Time-resolved observation and control of superexchange interactions with ultracold atoms in optical

- lattices. *Science* **319**, 295–299 (2008).
- <sup>8</sup> Simon, J. *et al.* Quantum simulation of antiferromagnetic spin chains in an optical lattice. *Nature* **472**, 307–312 (2011).
- <sup>9</sup> Struck, J. *et al.* Quantum simulation of frustrated classical magnetism in triangular optical lattices. *Science* **333**, 996–999 (2011).
- <sup>10</sup> Köhl, M., Moritz, H., Stöferle, T., Günter, K. & Esslinger, T. Fermionic atoms in a three dimensional optical lattice: observing Fermi surfaces, dynamics, and interactions. *Phys. Rev. Lett.* **94**, 080403 (2005).
- <sup>11</sup> Jördens, R., Strohmaier, N., Günther, K., Moritz, H. & Esslinger, T. A Mott insulator of fermionic atoms in an optical lattice. *Nature* **455**, 204–207 (2008).
- <sup>12</sup> Schneider, U. *et al.* Metallic and insulating phases of repulsively interacting fermions in a 3D optical lattice. *Science* **322**, 1520–1525 (2008).
- <sup>13</sup> Sachdev, S. Quantum magnetism and criticality. *Nature*

- Phys.* **4**, 173–185 (2008).
- <sup>14</sup> Tarruell, L., Greif, D., Uehlinger, T., Jotzu, G. & Esslinger, T. Creating, moving and merging Dirac points with a Fermi gas in a tunable honeycomb lattice. *Nature* **483**, 302–305 (2012).
  - <sup>15</sup> Uehlinger, T., Greif, D., Jotzu, G., Tarruell, L. & Esslinger, T. Double transfer through Dirac points in a tunable honeycomb optical lattice. *arXiv:1210.0904 [cond-mat.quant-gas]* (2012).
  - <sup>16</sup> Trotzky, S., Chen, Y.-A., Schnorrberger, U., Cheinet, P. & Bloch, I. Controlling and detecting spin correlations of ultracold atoms in optical lattices. *Phys. Rev. Lett.* **105**, 265303 (2010).
  - <sup>17</sup> Fuchs, S. *et al.* Thermodynamics of the 3D Hubbard model on approaching the Néel transition. *Phys. Rev. Lett.* **106**, 030401 (2011).
  - <sup>18</sup> Greif, D., Tarruell, L., Uehlinger, T., Jördens, R. & Esslinger, T. Probing nearest-neighbor correlations of ultracold fermions in an optical lattice. *Phys. Rev. Lett.* **106**, 145302 (2011).
  - <sup>19</sup> Jördens, R. *et al.* Quantitative determination of temperature in the approach to magnetic order of ultracold fermions in an optical lattice. *Phys. Rev. Lett.* **104**, 180401 (2010).
  - <sup>20</sup> Rüegg, C. *et al.* Pressure-induced quantum phase transition in the spin-liquid  $\text{TiCuCl}_3$ . *Phys. Rev. Lett.* **93**, 257201 (2004).
  - <sup>21</sup> Werner, F., Parcollet, O., Georges, A. & Hassan, S. R. Interaction-induced adiabatic cooling and antiferromagnetism of cold fermions in optical lattices. *Phys. Rev. Lett.* **95**, 056401 (2005).
  - <sup>22</sup> Mathy, C. J. M. & Huse, D. A. Accessing the Néel phase of ultracold fermionic atoms in a simple-cubic optical lattice. *Phys. Rev. A* **79**, 063412 (2009).
  - <sup>23</sup> Ma, P. N., Pilati, S., Troyer, M. & Dai, X. Density functional theory for atomic Fermi gases. *Nature Phys.* **8**, 601–605 (2012).
  - <sup>24</sup> Giamarchi, T. *Quantum Physics in One Dimension*. Oxford University Press, New York (2004).
  - <sup>25</sup> Gorelik, E. V. *et al.* Universal probes for antiferromagnetic correlations and entropy in cold fermions on optical lattices. *Phys. Rev. A* **86**, 061602(R) (2012).
  - <sup>26</sup> He, P.-B., Sun, Q., Li, P., Shen, S.-Q. & Liu, W. M. Magnetic quantum phase transition of cold atoms in an optical lattice. *Phys. Rev. A* **76**, 043618 (2007).
  - <sup>27</sup> Meng, Z. Y., Lang, T. C., Wessel, S., Assaad, F. F. & Muramatsu, A. Quantum spin liquid emerging in two-dimensional correlated Dirac fermions. *Nature* **464**, 847–851 (2010).
  - <sup>28</sup> Krauser, J. S. *et al.* Coherent multi-flavour spin dynamics in a fermionic quantum gas. *Nature Phys.* **8**, 613–618 (2012).
  - <sup>29</sup> Henderson, J. A., Oitmaa, J. & Ashley, M. C. B. High-temperature expansion for the single-band Hubbard model. *Phys. Rev. B* **46**, 6328 (1992).
  - <sup>30</sup> ten Haaf, D. F. B. & van Leeuwen, J. M. J. High-temperature series expansions for the Hubbard model. *Phys. Rev. B* **46**, 6313 (1992).

**Acknowledgements** We would like to thank Niels Blümer, Thierry Giamarchi, Corinna Kollath, Henning Moritz, Christian Rüegg, Manfred Sigrist, Niels Strohmaier and Shun Uchino for insightful discussions and Ulf Bissbort for help with the calculation of the Hub-

bard parameters in the dimerized lattice. We acknowledge SNF, NCCR-QSIT, NCCR-MaNEP, and SQMS (ERC advanced grant) for funding.

**Author Contributions** The data was taken and analysed by D.G., T.U., G.J. and L.T. The experimental concept was developed by T.E. All authors contributed extensively to the discussion of the results, as well as to the preparation of the manuscript.

**Author Information** Correspondence and requests for materials should be addressed to T.E. (esslinger@phys.ethz.ch).

## SUPPLEMENTARY INFORMATION

### A. Dimerized cubic lattice - series expansion

We start with the definition of the homogeneous single-band Hubbard Hamiltonian in a dimerized cubic lattice with strong and weak links between nearest neighbours  $\langle i, j \rangle_{\blacksquare}$  and  $\langle i, j \rangle_{\blacktriangle}$  respectively, see Fig. 5,

$$\begin{aligned}\hat{H}_D &= \hat{H}_o + \hat{H}_c \\ \hat{H}_o &= -t_d \sum_{\sigma, \langle i, j \rangle_{\blacksquare}} (\hat{c}_{i, \sigma}^\dagger \hat{c}_{j, \sigma} + \text{h.c.}) + U \sum_i \hat{n}_{i\uparrow} \hat{n}_{i\downarrow} \\ &\quad - \mu \sum_i (\hat{n}_{i\uparrow} + \hat{n}_{i\downarrow}) \\ \hat{H}_c &= -t \sum_{\sigma, \langle i, j \rangle_{\blacktriangle}} (\hat{c}_{i, \sigma}^\dagger \hat{c}_{j, \sigma} + \text{h.c.}).\end{aligned}\quad (6)$$

We have split the Hamiltonian into the dimer part  $\hat{H}_o$  and the coupling between dimers  $\hat{H}_c$ . The on-site interaction energy is given by  $U$ , the tunnelling matrix elements between nearest neighbours by  $t$  and  $t_d$  and the chemical potential is parametrized with  $\mu$ . The fermionic creation operator for an atom on the lattice site  $i$  is given by  $\hat{c}_{i\sigma}^\dagger$ , where  $\sigma \in \{\uparrow, \downarrow\}$  denotes the magnetic sublevel and h.c.

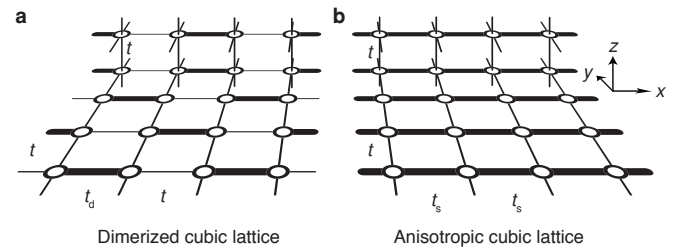


**FIG. 5. Lattice geometries.** Overview of the three-dimensional lattice geometries explored in the experiment. **a**, In the dimerized cubic lattice the tunnelling between neighbouring sites is increased to  $t_d$  on a chequerboard pattern in the  $xy$  plane as compared to the weaker tunnelling  $t$ . The pattern replicates along the  $z$  axis. **b**, In the anisotropic cubic lattice the tunnelling is increased to  $t_s$  along the  $x$  axis, while remaining  $t$  in the other two directions.

is the Hermitian conjugate. The particle number operator is  $\hat{n}_i = \hat{n}_{i\uparrow} + \hat{n}_{i\downarrow}$ ,  $\hat{n}_{i\sigma} = \hat{c}_{i\sigma}^\dagger \hat{c}_{i\sigma}$ . Denoting the inverse temperature with  $\beta = 1/k_B T$ , the thermal average of an observable  $\mathcal{O}$  then reads in the grand canonical potential

$$\langle \mathcal{O} \rangle = \frac{\text{Tr}\{\mathcal{O} e^{-\beta \hat{H}_D}\}}{\text{Tr}\{e^{-\beta \hat{H}_D}\}}. \quad (7)$$

We now treat the coupling Hamiltonian  $\hat{H}_c = t\hat{T}$  as a perturbation, which leads to an expansion of the above expression in powers of the dimensionless parameter  $\beta t$  (ref. 29 in the main text). The expansion is expected to be close to the exact result in the regime  $t \ll k_B T \ll t_d, U$ . For the partition function up to second order (denominator in Eq. 7) we find

$$\mathcal{Z} = \mathcal{Z}_0 + (\beta t)^2 \frac{\mathcal{Z}_0}{\beta^2} \int_0^\beta \int_0^{\tau_1} d\tau_2 d\tau_1 \langle \hat{T}'(\tau_1) \hat{T}'(\tau_2) \rangle_0. \quad (8)$$

The expression for the numerator is analogous. The partition function of the unperturbed Hamiltonian is denoted by  $\mathcal{Z}_0$ , whereas  $\langle \dots \rangle_0$  denotes the thermal average of the unperturbed Hamiltonian

$$\begin{aligned} \langle \hat{T}'(\tau_1) \hat{T}'(\tau_2) \rangle_0 &= \text{Tr}\{\exp(-\beta \hat{H}_0) \hat{T}'(\tau_1) \hat{T}'(\tau_2)\} / \mathcal{Z}_0 \\ \hat{T}'(\tau) &= e^{\tau \hat{H}_0} \hat{T} e^{-\tau \hat{H}_0}. \end{aligned} \quad (9)$$

### B. Dimerized cubic lattice - observables

As the expansion is up to second order in the tunnel coupling, it is sufficient to evaluate all expressions in a two-dimer basis. Denoting the single dimer Hamiltonian in the grand canonical potential with  $\hat{H}_0^s$ , the unperturbed partition function then reads

$$\mathcal{Z}_0 = \left( \text{Tr}\{e^{-\beta \hat{H}_0^s}\} \right)^2. \quad (10)$$

The evaluation of the second order terms is done in a double dimer basis  $|\Psi_i^1, \Psi_j^2\rangle$ , where  $|\Psi_i^1\rangle$  and  $|\Psi_j^2\rangle$  each denote one of the 16 possible eigenvectors of the first and second dimer link. This essentially leaves the evaluation of matrix elements of the following kind

$$\begin{aligned} \langle \Psi_j^2, \Psi_i^1 | \hat{T}'(\tau_1) \hat{T}'(\tau_2) | \Psi_i^1, \Psi_j^2 \rangle \quad \text{and} \\ \langle \Psi_j^2, \Psi_i^1 | \mathcal{O} \hat{T}'(\tau_1) \hat{T}'(\tau_2) | \Psi_i^1, \Psi_j^2 \rangle, \end{aligned} \quad (11)$$

which can be computed either directly or numerically. For the singlet and triplet fraction the observable  $\mathcal{O}$  takes the form of a projector for the 16 possible states on a dimer. The entropy and particle number per dimer are evaluated from the grand canonical potential  $\Omega_d = -k_B T \log \mathcal{Z}_d$  of a single dimer. Fig. 6 shows the dimer singlet probability and the entropy per site versus filling calculated in second order for different temperatures and dimerizations. A comparison between the predictions of lowest order (atomic limit) and second order is shown in Fig. 7.

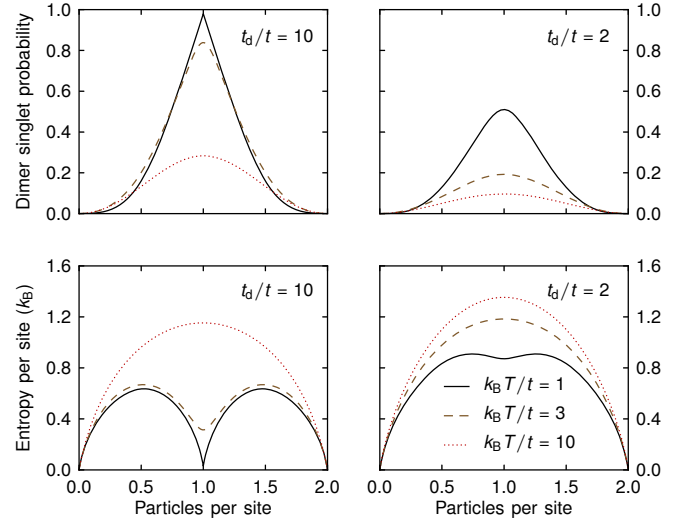


FIG. 6. **Dimerized lattice.** High-temperature series predictions up to second order for the homogeneous dimerized cubic lattice. The dependence on filling of the dimer singlet probability and of the entropy per site is shown. We set  $U/t = 5$  and  $t_d/t = 10$  or  $2$  and use different temperatures  $k_B T/t$ . The entropy at half filling for large dimerization is strongly reduced.

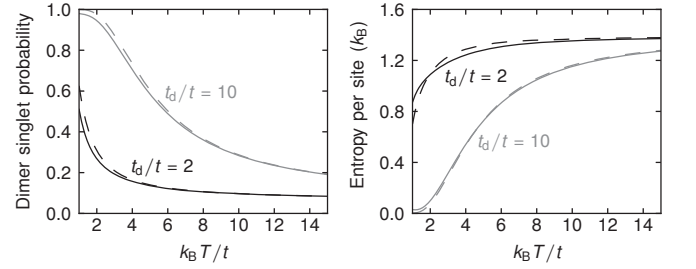


FIG. 7. **Higher order contributions.** Comparison of the high-temperature series predictions in lowest and second order (dashed and solid line) for the dimer singlet probability and for the entropy per site in a homogeneous dimerized cubic lattice. The filling is set to one particle per site and the interaction to  $U/t = 5$ . The second order contributions are expected to be larger for lower temperatures and lead to a reduction of the singlet probability.

### C. Anisotropic cubic lattice

Similar to the case of the dimerized lattice, we split the Hamiltonian for the homogeneous anisotropic cubic lattice into two parts

$$\begin{aligned} \hat{H}_A &= \hat{H}_U + \hat{H}_t \\ \hat{H}_U &= U \sum_i \hat{n}_{i\uparrow} \hat{n}_{i\downarrow} - \mu \sum_i (\hat{n}_{i\uparrow} + \hat{n}_{i\downarrow}) \end{aligned} \quad (12)$$

$$\hat{H}_t = -t_s \sum_{\sigma, \langle i, j \rangle_{\perp}} (\hat{c}_{i, \sigma}^\dagger \hat{c}_{j, \sigma} + \text{h.c.}) - t \sum_{\sigma, \langle i, j \rangle_{\parallel}} (\hat{c}_{i, \sigma}^\dagger \hat{c}_{j, \sigma} + \text{h.c.}).$$

Notations are analogous to the previous section, see Fig. 5. The strong tunnelling between nearest neigh-



bours along the  $x$  direction is denoted with  $t_s$ , whereas the weaker tunnelling along the other two axes is given by  $t$ . We treat the tunnelling Hamiltonian  $\hat{H}_t$  as a perturbation to the unperturbed part  $\hat{H}_U$ , which leads to an expansion of the partition function as in Eq. 8 in powers of  $\beta t_s$  and  $\beta t$ . Density and entropy per site are then obtained from derivatives of the second order grand potential  $\Omega$ ,

$$\beta\Omega = -\log Z_1 - \frac{2(\beta t_s)^2 + 4(\beta t)^2}{(Z_1)^2} \left( \zeta + \zeta^3 w + 2\zeta^2 \frac{1-w}{\beta U} \right). \quad (13)$$

Here  $Z_1$  is the unperturbed single site partition function,  $\zeta = \exp(\beta\mu)$  the fugacity and  $w = \exp(-\beta U)$ .

The evaluation of the two correlators defined in the main text  $\langle S_i^z S_{i+1}^z \rangle$  and  $\mathcal{S}$  is slightly more complicated, as it involves two neighbouring sites. However, the coefficients for these correlators have already been computed (ref. 30 in the main text).

$$\langle S_i^z S_{i+1}^z \rangle = -\frac{\zeta^2}{(Z_1^s)^2} \left( \frac{1}{\beta U} + \frac{w-1}{(\beta U)^2} \right) (\beta t_s)^2 \quad (14)$$

$$\mathcal{S} = \left( \frac{1}{\beta U} + \frac{w-1}{(\beta U)^2} \right) (\beta t_s)^2. \quad (15)$$

#### D. Harmonic trap

The effect of the harmonic trap is included in a local density approximation with a quadratically varying chemical potential

$$\mu(r) = \mu_0 - \frac{1}{2} m \bar{\omega}^2 \left( \frac{\lambda}{2} \right)^2 r^2, \quad (16)$$

where  $\bar{\omega}$  is the geometric mean of the trapping frequencies,  $\mu_0$  the chemical potential in the centre of the trap and  $r$  the normalized distance of a site to the trap centre. Any trap averaged observable  $\mathcal{O}^{\text{trap}}$  is then obtained from integration of the contributions per site  $\mathcal{O}^{\text{hom}}(\mu)$

$$\mathcal{O}^{\text{trap}} = \int_0^\infty 4\pi r^2 \mathcal{O}^{\text{hom}}(\mu(r)) dr. \quad (17)$$

Owing to the harmonic trap, the energy offset between neighbouring sites on the dimer links changes over the cloud size. The relative correction of this effect to all shown quantities was computed to be less than a few percent.

#### E. Singlet and triplet fractions

The fraction of atoms forming singlets and triplets  $p_s$  and  $p_{t_0}$  are obtained from an integration over the left merging sites, which are denoted by  $\mathcal{A}$  (as described in

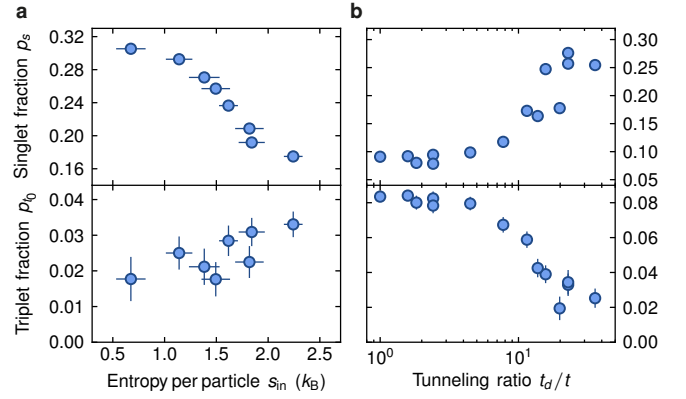


FIG. 8. **Dimerized simple cubic lattice.** **a**, Singlet and triplet fractions on the strong dimer links vs. initial entropy before loading into the lattice. The data shown here is used to compute the normalized imbalance  $\mathcal{I}$  displayed in Fig. 3a. **b**, Singlet and triplet fractions as a function of dimerization  $t_d/t$ , corresponding to the measurements of Fig. 3b. Vertical error bars denote the fit error from singlet-triplet oscillations consisting of 63 measurements, the errors in  $t_d/t$  stem from lattice calibration uncertainties and the errors in  $s_{\text{in}}$  are the standard deviation of five measurements.

the main text, see Fig. 2b)

$$p_s = 2 \sum_{i \in \mathcal{A}} \langle \hat{P}_i^s \rangle / N \quad \hat{P}_i^s = |\Psi_i^s\rangle \langle \Psi_i^s| \quad (18)$$

$$p_{t_0} = 2 \sum_{i \in \mathcal{A}} \langle \hat{P}_i^{t_0} \rangle / N \quad \hat{P}_i^{t_0} = |\Psi_i^{t_0}\rangle \langle \Psi_i^{t_0}|. \quad (19)$$

Here  $\hat{P}_i^s$  and  $\hat{P}_i^{t_0}$  are the projection operators on the singlet and triplet states  $|\Psi_i^s\rangle$  and  $|\Psi_i^{t_0}\rangle$  on neighbouring sites  $i$  and  $i+1$ ,  $\langle \dots \rangle$  denotes the thermal average and  $N$  the total atom number. For the measurements in the anisotropic simple cubic lattice, the projection operators are related to the spin operators  $\vec{S}_i = 1/2 \sum_{s,s'} \hat{c}_{i,s}^\dagger \vec{\sigma} c_{i,s'}$ , where  $\vec{\sigma} = (\sigma_x, \sigma_y, \sigma_z)$  are the Pauli matrices

$$\hat{P}_i^s = \frac{\hat{n}_i \hat{n}_{i+1}}{4} - \vec{S}_i \vec{S}_{i+1} \quad (20)$$

$$\hat{P}_i^{t_0} = \vec{S}_i \vec{S}_{i+1} - 2S_i^z S_{i+1}^z + \frac{\hat{n}_i \hat{n}_{i+1}}{4}. \quad (21)$$

From this the equality of Eq. 2 in the main text is immediately obtained. In the dimerized lattice the projection operator on the triplet reads the same, whereas for the singlet the two-site system needs to be diagonalized.

Fig. 8 shows the individual atomic fractions of singlets and triplets ( $p_s$  and  $p_{t_0}$ ) measured in the dimerized lattice, which are used to compute the normalized imbalance  $\mathcal{I}$ . The data in Fig. 8a corresponds to the entropy scan of Fig. 3a in the main text, whilst the set of measurements for different tunnelling ratios in Fig. 8b corresponds to Fig. 3b. We additionally measured the fraction of atoms on doubly occupied sites  $D$  in the lattice after freezing out the atomic motion but before applying the cleaning procedure and inducing singlet-triplet

oscillations. For the entropy scan we find a nearly constant value of  $D = 0.026(5)$ . For the measurements taken at different  $t_d/t$  the double occupancy ranges between 0.066(4) and 0.29(2).

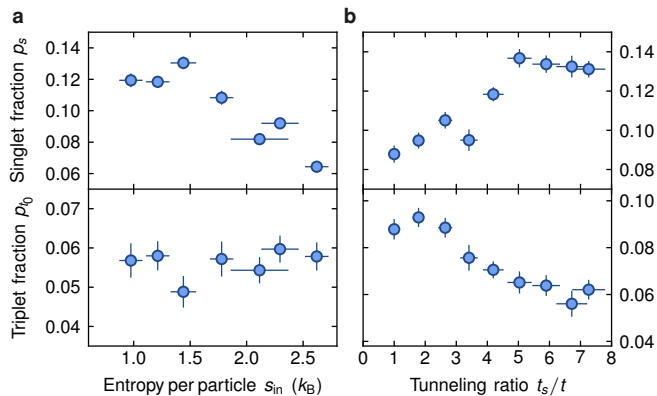


FIG. 9. **Anisotropic simple cubic lattice.** **a**, Singlet and triplet fractions as a function of initial entropy before loading into the lattice, corresponding to the measurements of Fig. 4b. **b**, Singlet and triplet fractions vs. tunnelling anisotropy  $t_s/t$ , which are used to compute the spin correlators presented in Fig. 4a. Vertical error bars denote the fit error from singlet-triplet oscillations consisting of 63 measurements, the errors in  $t_s/t$  stem from lattice calibration uncertainties and the errors in  $s_{in}$  are the standard deviation of five measurements.

Fig. 9 shows  $p_s$  and  $p_{t_0}$  for the measurements in the anisotropic cubic lattice, which are used to compute the spin correlators  $-\langle S_i^x S_{i+1}^x \rangle - \langle S_i^y S_{i+1}^y \rangle$  and  $\mathcal{S}$ . Fig. 9a corresponds to the measurements versus entropy displayed in Fig. 4b, whilst the scan of the tunnelling anisotropy shown in Fig. 9b corresponds to the data presented in Fig. 4a. For the entropy scan  $D$  lies between 0.11(6) and 0.21(1), whilst for the scan of  $t_s/t$  we measure double occupancies between 0.14(2) and 0.19(2).